ACS APPLIED MATERIALS & INTERFACES

Research Article

Cite This: ACS Appl. Mater. Interfaces 2017, 9, 38187-38200

www.acsami.org

Direct Writing Electrospinning of Scaffolds with Multidimensional Fiber Architecture for Hierarchical Tissue Engineering

Honglin Chen,[†] Afonso de Botelho Ferreira Braga Malheiro,[†] Clemens van Blitterswijk, Carlos Mota, Paul Andrew Wieringa, and Lorenzo Moroni*

Department of Complex Tissue Regeneration, MERLN Institute for Technology-Inspired Regenerative Medicine, Maastricht University, 6200 MD Maastricht, The Netherlands

Supporting Information

ABSTRACT: Nanofibrous structures have long been used as scaffolds for tissue engineering (TE) applications, due to their favorable characteristics, such as high porosity, flexibility, high cell attachment and enhanced proliferation, and overall resemblance to native extracellular matrix (ECM). Such scaffolds can be easily produced at a low cost via electrospinning (ESP), but generally cannot be fabricated with a regular and/or complex geometry, characterized by macropores and uniform thickness. We present here a novel technique for direct writing (DW) with solution ESP to produce complex three-dimensional (3D) multiscale and ultrathin (~1 μm) fibrous scaffolds with desirable patterns and geometries. This technique was simply achieved via manipulating technological conditions, such as spinning solution, ambient conditions, and processing parameters. Three different regimes in fiber morphologies were observed, including bundle with dispersed fibers, bundle with a core of aligned fibers, and single fibers. The transition between these regimes depended on tip to collector distance (Wd) and applied voltage (V), which could be simplified as the ratio V/Wd. Using this technique, a scaffold mimicking the zonal organization of articular cartilage was further fabricated as a proof of concept, demonstrating the ability to better mimic native tissue organization. The DW scaffolds directed tissue organization and fibril matrix orientation in a zone-dependent way. Comparative expression of chondrogenic markers revealed a substantial upregulation of *Sox9* and aggrecan (ACAN) on these structures compared to conventional electrospun meshes. Our novel method provides a simple way to produce customized 3D ultrathin fibrous scaffolds, with great potential for TE applications, in particular those for which anisotropy is of importance.

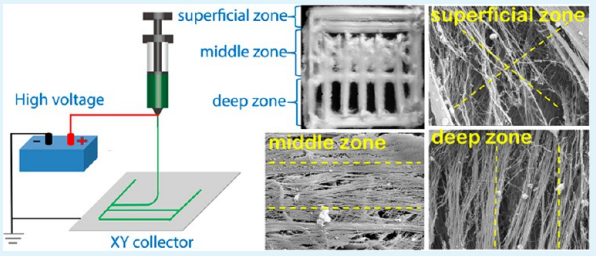

KEYWORDS: *direct writing, electrospinning, tissue engineering, articular cartilage, human mesenchymal stromal cells*

1. INTRODUCTION

Tissue engineering (TE) is a promising approach to replace the currently suboptimal clinical treatments aiming to restore the function of damaged or diseased tissues and organs. Additive manufacturing (AM) techniques have greatly contributed to this goal. These technologies have provided valuable tools for the custom fabrication of 3D scaffolds with reproducible patterns, tunable porosity, and tailored physicochemical properties.[1] However, limitations inherent to these processes still persist. Notably, the required setups are typically expensive, and the range of usable materials is dependent on the fabrication technique, for instance, extrudable thermoplastic polymers for fused deposition modeling. These techniques also introduce other concerns, such as thermal degradation of the polymer during the fabrication process.[1] Moreover, current AM techniques possess low spatial resolution, and thus, the features of the produced scaffolds are typically several orders of magnitude larger than extracellular matrix (ECM) fibers, particularly collagen fibrils. This results in a poor cell-seeding efficiency and proliferation, as well as nonuniform scaffold coverage.

Nanofibrous scaffolds are interesting alternatives for TE, with a highly porous structure reminiscent of the ECM milieu that has been shown to promote cell attachment and to stimulate cell function while the efficient exchange of nutrients, oxygen, and metabolites is facilitated.[2] Nanofibers are also very flexible due to their high aspect ratio, allowing cells to remodel their surroundings with produced matrix.[3] To fabricate nanofibrous mats, solution electrospinning (ESP) is one of the most popular methods, since it is easy to operate, relatively inexpensive, and versatile in terms of materials selection.[4] ESP is a complex hydrodynamic process governed by many variables and characterized by an unpredictable electrified jet.[5] The chaotic nature of this jet results from the buildup of surface charges generated by an applied electrostatic force, which initially leads to droplet elongation, Taylor cone formation, and jet emanation, but soon overcomes the liquid surface tension, causing bending instabilities.[5,6] As charge density increases, repulsion forces alter the stable jet into a whipping jet. At this

Received: May 20, 2017
Accepted: October 18, 2017
Published: October 18, 2017

DOI: 10.1021/acsami.7b07151
ACS Appl. Mater. Interfaces 2017, 9, 38187–38200

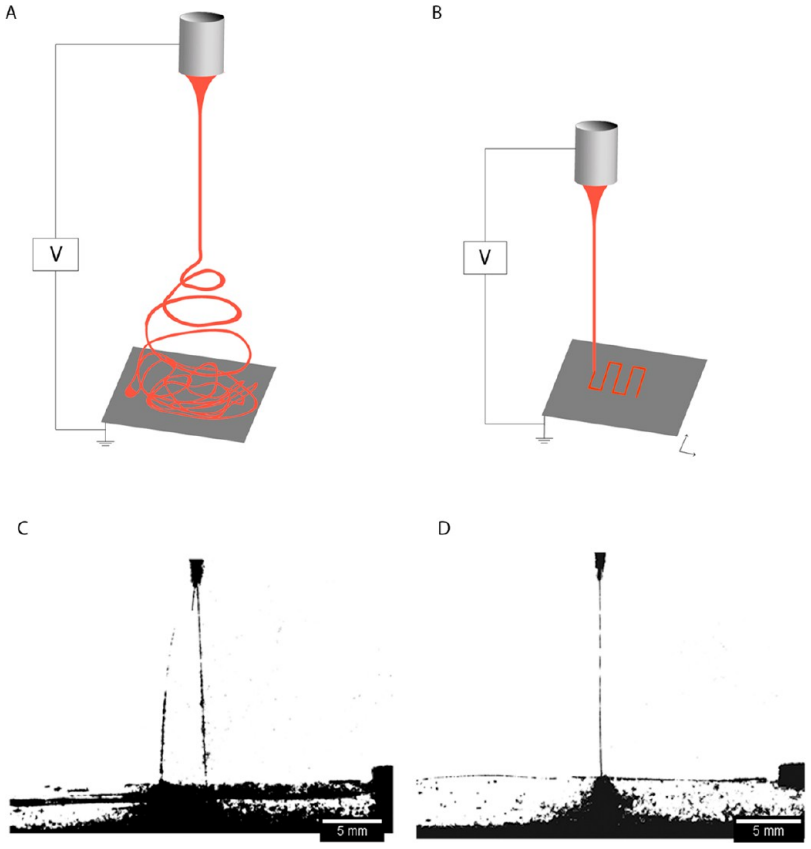

Figure 1. Illustration of the ESP process in conventional (A) and direct writing (B) mode. In direct writing mode, the jet travels in a straight path and the translational stage moves in *X* and *Y* directions to create a pattern. Photos of an electrified jet when traveling with an unfocused trajectory (C; V = 7 kV and Wd = 3 cm) and in stable path (D; V = 5 kV and Wd = 3 cm).

point, fiber deposition occurs randomly and thus accurate pattern designing is impeded. Therefore, most ESP products are dense meshes that lack a regular pore-size network and have an architecture defined by the collector shape (e.g., flat or grooved plate, rotating drums, and spaced electrodes).[6,7]

Achieving control over ESP fiber deposition would enable ESP in a direct writing (DW) mode, which provides the combined benefits of the topography provided by electrospun mats with the reproducibility and designing potential of AM techniques. Therefore, much interest has been taken in the pursuit of DW ESP via different approaches, including improving jet focusing using additional devices, reducing working distance, and melt ESP.[8−10] Through the use of a ring electrode positioned between the spinneret and collector, Neubert et al. and Bellan and Craighead showed the targeted deposition of fibers into a single spot.[11,12] By either moving the collector or using steering electrodes, simple lines could be patterned onto the collector, but no complex patterning was achieved, A similar but improved strategy was followed by Lee et al., who employed a side-wall electrode, a thin glass plate collector, and a sharp-pin electrode to focus the electrified jet and draw regular 3D nanofibrous patterns,[9] which could later be stacked to build a larger scaffold.[13] Although successful, the aforementioned approach relied on a complex setup that is difficult to adopt in other laboratories. An earlier and simpler approach that dispenses additional setup modifications is near-field ESP, in which the unstable region of the jet is bypassed, by closely approximating the spinneret to the collector and using very low voltages.[10,14,15] However, drawbacks to this technique are evident, as it relies on a solution-dipped probe for jet feeding, which greatly limits the possible scaffold size. In the case of melt ESP, polymer solution was replaced with a molten polymer to generate fibers.[8,16] Application of melt ESP for DW of poly(ε-caprolactone) (PCL) fibrous structures for hydrogel reinforcement has revealed great potential in engineered cartilage constructs.[17] This technique has been also used to fabricate cell-invasive 3D scaffolds constructed from photo-cross-linkable poly(L-lactide-*co*-ε-caprolactone-*co*-acryloyl carbonate) microfibers.[18,19] Because of the use of high melting temperatures, the technique may cause polymer degradation and is restricted to the use of thermoplastic polymers. In addition, it excludes the addition of bioactive molecules, such as collagen, which undergo denaturation at high temperatures.[16,20] The minimum feature size is also a concern in melt ESP, since the Barus effect induces a jet enlargement[21] and obstructs formation of nanofibers, although recent efforts have shown the production of submicron fibers under special conditions.[22] This process also produces a single fiber at a time, while tissue development benefits from the presence of multiple interconnected fibers that act as anchoring points for cells to assemble focal adhesions.[23] The comparison of current techniques for direct-write ESP is summarized in Table S1 of the Supporting Information (SI).

To overcome all of the above-mentioned problems, we show here the development of a novel DW technique that allows conventional solution ESP to focus the jet to a single point and collect fibers in a dry state. We achieved this goal through optimizing conditions for DW ESP, including solution, ambient conditions, and processing parameters. Patterns could be designed via predefining *XY* translation of the collector, and

DOI: 10.1021/acsami.7b07151
ACS Appl. Mater. Interfaces 2017, 9, 38187−38200

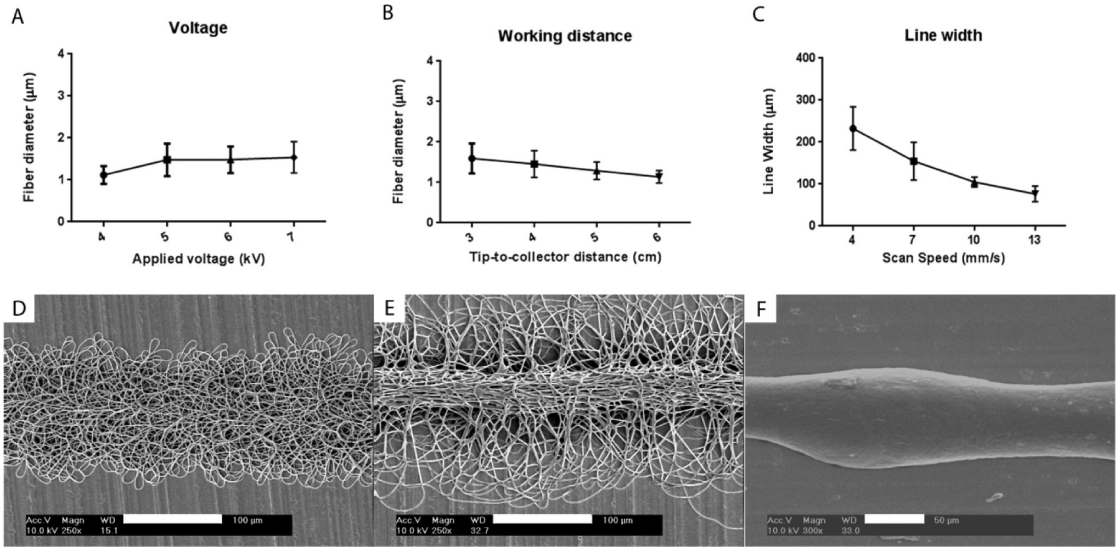

Figure 2. Influence of the ESP processing parameters on fiber diameter (A and B) and line width (C). Applied voltage (A), working distance (B), and collector speed (C) were varied. SEM micrographs of different possible configurations of the fiber bundle within the DW range: (D) bundle with dispersed fibers (V = 5 kV and Wd = 3 cm), (E) bundle with a core of aligned fibers (V = 6 kV and Wd = 3 cm), and (F) single fiber (V = 4.5 kV and Wd = 2 cm). Scale bars: D and E, 100 μm; F, 50 μm.

the resulting fibers are stacked to create 3D constructs. After characterizing this technological process, scaffolds that mimic the zonal configuration of articular cartilage were fabricated as a proof of concept, demonstrating the ability to better mimic native tissue hierarchical organization. These scaffolds were seeded with human mesenchymal stromal cells (hMSCs) and cultured in chondrogenic differentiation medium over the course of 21 days. The DW ESP scaffolds successfully supported hMSCs proliferation and early chondrogenic differentiation, as evaluated by matrix production and orientation, tissue development, and gene expression. These data argue that DW ESP can fabricate ultrathin scaffolds with multidimensional fiber architecture and favorable biological characteristics, which has great potential for wide TE applications.

2. RESULTS AND DISCUSSION

Traditional ESP generally deposits fibers with random morphology due to the bending instability of the electrospinning jet (Figure 1A). However, controlled fiber deposition, and thus patterning, is possible by DW with ESP and requires the jet to follow a stable path from the moment it emanates from the spinneret tip until it reaches the collector (Figure 1B). To fabricate suitable scaffolds to mimic articular cartilage, we deployed DW with ESP. First, we optimized the ESP process for DW, including polymer solution, flow rate, applied voltage, working distance, and ambient conditions.

2.1. Solution Conditions. For these studies, we used a polymer solution of poly(ethylene oxide terephthalate)/poly(butylene terephthalate) (PEOT/PBT) for the scaffolds, because it has been demonstrated as a biocompatible and degradable polymer with promising application for skeletal regeneration.[24,25] Elongation and stability of the ESP jet depends on optimal solution parameters. Solutions with a very high viscosity usually exhibit longer stress relaxation times, which can prevent fracturing of the jet during ESP.[6] We tested solution mixtures with polymer concentrations between 26 and 30% (w/v) and $CHCl_3$:HFIP solvent ratios between 70:30 and 80:20 (v/v). We found that the optimal range of polymer concentration that permits DW was 27−29% (w/v), which yielded fairly viscous solutions. The optimal range of solvent ratio that permits DW was between 74:26 and 78:22 (v/v), which ensured good polymer dissolution and yielded a solution with a high evaporation rate. A solution with a high evaporation rate is particularly important for the DW technique, since it enables fibers to dry quickly within shorter working distances (Wd) used in these studies. Within the optimal range of polymer concentration and solvent ratio, the solution with 28% (w/v) polymer in 75:25 $CHCl_3$/HFIP (v/v) revealed the best outcome for a stable and continuous DW process (Table S2, SI).

2.2. Solution Flow Rate. The solution flow rate through the spinneret is an important factor, as it influences the amount of transferred material and jet velocity.[6] We tested flow rates from 0.05 to 2 mL/h. We found that flow rates between 0.08 and 0.3 mL/h, a range that enables a low but steady flow of the polymer solution through the spinneret, were necessary for successful DW ESP. The influence of flow rates (0.05, 0.1, and 0.5 mL/h) on the jet and fiber deposition is shown in Figure S1A−C (SI) to exemplify the conditions tested. At a low flow rate of 0.05 mL/h, the amount of solution that was supplied through the spinneret was insufficient to maintain a regular jet for the applied voltage (8 kV) and scan speed, thus leading to the deposition of an erratic line (Figure S1A, SI). As the flow rate increased to 0.1 mL/h, a thin and steady jet was produced, resulting in the formation of straight line patterns (Figure S1B, SI). When the polymer solution supply was 0.5 mL/h, the jet could no longer be focused, and consequently, the result was the collection of dispersed fiber mesh (Figure S1C, SI). Thus, we concluded that the optimal flow rate was ∼0.1 mL/h.

2.3. Applied Voltage and Working Distances. In addition to the solution conditions and flow rate, the interplay between the applied voltage and the distance from the collector affects the solution jet. The applied voltage needs to reach a certain threshold to initiate the ESP process.[5,26] As the voltage increases, the solution ejection also increases and higher electrostatic repulsive forces build up on the fluid jet.[5,6] The optimal applied voltage is also dependent on the Wd, as both parameters are related in the determination of the electric field

DOI: 10.1021/acsami.7b07151
ACS Appl. Mater. Interfaces 2017, 9, 38187−38200

strength.[27] A typical electrified jet will follow a short stable path before acquiring a whipping profile;[28] thus selecting an appropriate Wd is of utmost importance. We tested applied voltages between 2 and 16 kV, with corresponding Wd values between 2 and 12 cm. The threshold voltages needed to initiate the ESP process increased as the Wd increased: the minimum voltages were 4 kV at 2 cm, 4.5 kV at 3 cm, and 5.5 kV at 4 cm (Table S3, SI). It is worth mentioning that following jet initiation, the spinning voltage could be reduced to a value lower than its jet initiation voltage. For example, at 2 cm, the lowest Wd tested, the minimum voltage for jet initiation was 4 kV during DW ESP. However, following jet initiation, the spinning voltage could be reduced to a minimum value of 2.5 kV. At 7 kV and a Wd of 3 cm, we observed an unfocused jet, which broke down into multiple thin jets as a consequence of jet bending instability (Figure 1C). In this case, the amount of ejected solution provided insufficient viscoelastic force to balance surface charge density.[29] When we deceased the voltage to 5 kV, a stable jet was achieved during its flight time (Figure 1D), depositing and vertically building the fibers in a single point in the static collector. However, this process could not continue indeterminably due to an increase in charge accumulation, resulting in an increase of repulsive forces at that point (Figure S2, SI). We then increased the Wd to 8 cm and tested different applied voltages. At 8 kV, the jet trajectory was stable and straight lines could be fabricated (Figure S1D, SI). At 12 kV, the amount of ejected fluid increased, resulting in too much volume at the collector to produce single steady lines at the given scan speed (Figure S1E, SI). At 16 kV, the repulsive charges accumulated and led to the onset of bending instabilities, resulting in the complete loss of the focusing effect (Figure S1F, SI). When the Wd was further increased to 10 and 12 cm, either the jet was collected in its whipping phase or the electric field strength was too low to focus it, resulting in unpredictable fiber deposition (Figure S1H,I, SI). From these data, we concluded that Wd $\leq$ 8 cm and voltages $\leq$ 8 kV were necessary to collect the jet in a stable and focusing manner.

From voltage and Wd parameters that resulted in successful focused spinning, we examined the morphology of the deposited fibers (Table S3, SI) and found three different regimes (Figure 2D−F). The transition between these regimes depended both on Wd and electrical field strength derived from the applied voltage (V), which could be simplified as the ratio V/Wd. Typically, for low V/Wd, the fibers were randomly deposited in a bundle and dispersed from each other (Figure 2D). As the V/Wd ratio increased, there was an improvement in fiber alignment, the fiber density increased and the distance between fibers decreased, resulting in increased fiber cohesiveness [Table S5 (SI) and Figure 2E]. If the V/Wd ratio was increased by increasing the voltage, the fiber bundle displayed a more three-dimensional core, with the fibers aligned in the direction of the jet movement, as well as a thicker fiber dimension [Figures 2A and S3 (SI)]. If the V/Wd ratio was increased via reducing the Wd, similar morphological changes were achieved together with an increase of fiber diameter [Figure 2B and S4 (SI)]. Reducing the Wd lead to less fiber dispersion, and thus better alignment, compared to voltage change (Table S5 and Figures S3 and S4, SI). The transition between a random deposition (lower limit) and an anisotropic alignment (upper limit) can then be defined by the V/Wd ratio, suggesting that these morphological changes are determined by an interplay between the jet travel distance and the amount of solution ejected. In specific situations, if the V/Wd ratio is further increased and the Wd is low, the jet may not spin and the resulting morphology is a single fiber (Figure 2F). For example, at a Wd of 2 cm, an applied voltage of 4.5 kV (V/Wd > 2) resulted in single fiber deposition. However, this was only possible at Wd $\leq$ 2 cm, since the threshold that defines the balancing of repulsive charges by the solution cohesive forces is also low.

2.4. Scan Speed. The velocity at which the fibers were collected was also a parameter of great interest. If the voltage and Wd were maintained constant, the physical behavior of the jet would be in principle the same. However, the velocity at which the jet or collector moves would influence the amount of fibers reaching a single point on the collector. Consequently, the amount of charges in a single spot can also vary and can determine the consistency of the fiber deposition. We maintained the voltage at 5 kV and Wd at 5 cm but varied the scan speed between 4 and 10 mm/s to determine its effect on the deposited fibers (Figure S5, SI). At a collection speed of 4 mm/s, the deposited layer was slightly incoherent with respect to its central axis and some fiber dispersion occurred. When the scan speed was increased to 7 mm/s, the accumulation of repulsive charges at a point decreased and the spun layer showed a more consistent pattern, but still presented some fiber dispersion from its core (Figure S5B, SI). At a collection speed of 10 mm/s, the deposited layer showed little deviation from its central axis having comparatively less fiber dispersion (Figure S5C, SI). However, the morphology of the deposited layer did not significantly change if the collection speed was above 10 mm/s (data not shown). In summary, as the collector scan speed increased, the line focusing was improved, whereas line patterns assumed a proportionally shorter width (Figure 2C). From these data, we conclude that a scan speed above 10 mm/s was necessary to maintain a focusing deposited layer when the voltage applied was kept at 5 kV

2.5. Ambient Parameters. Finally, the ambient parameters for ESP, such as temperature and relative humidity, were also important to control. Since an inverse relationship exists between temperature and viscosity (crucial for jet elongation, as mentioned above),[30] we reasoned that lower temperatures would facilitate jet focusing and relative higher temperatures may cause faster solvent evaporation and, consequently, needle blocking by the polymer solution. Therefore, we tested temperatures between 18.5 and 30 °C and found the optimal temperature to be ∼20 °C.

Relative humidity within the fairly large range of 25−55% allows for jet eruption and focusing, but we needed to optimize this parameter for long fabrication times. The production of large patterns requires the hemispherical drop at the spinneret tip to be maintained in a fluid state, which is facilitated by humidity levels. Furthermore, solutions containing volatile solvents may dry quickly in dry environments. High humidity also benefits fiber stacking by reducing the charge accumulation. It should be noted that excessive humidity results in melting the fiber morphology due to insufficient solvent evaporation. From the humidity tested, we found that the optimal relative humidity was 40 ± 2%.

2.6. Optimal ESP Parameters. The range of processing parameters that permitted DW ESP of PEOT/PBT is summarized in Table S4 (SI). We found that the optimal range of polymer concentration was from 27 to 29% (w/v), which yielded fairly viscous solutions. Wd values of ≤8 cm were necessary to collect the jet in its stable region, with

DOI: 10.1021/acsami.7b07151
ACS Appl. Mater. Interfaces 2017, 9, 38187−38200

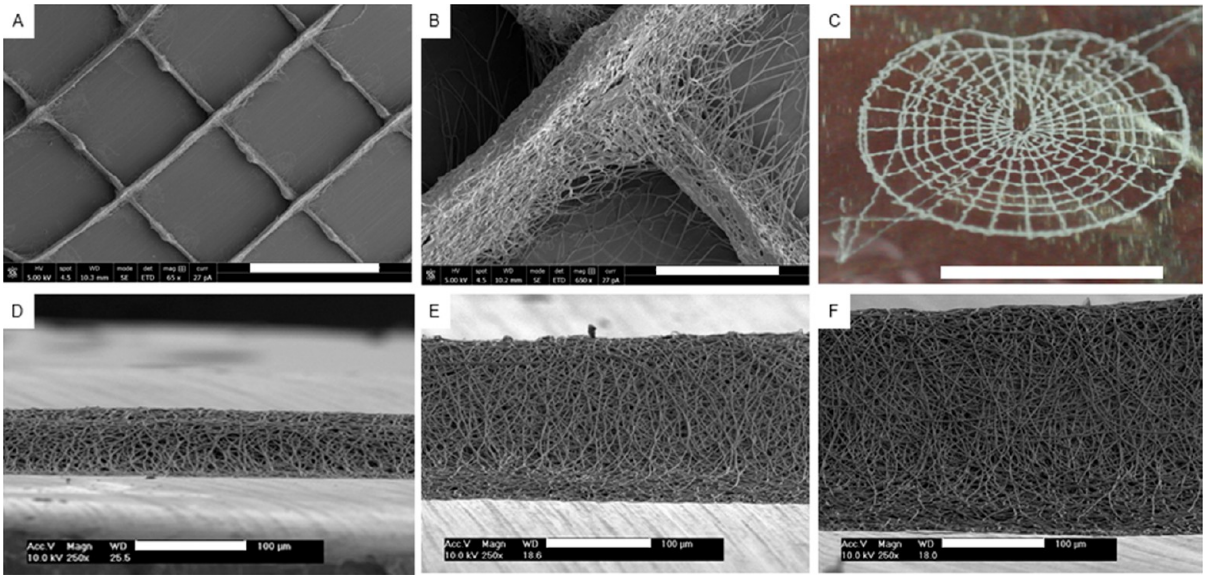

Figure 3. Pattern fabrication with DW ESP. SEM micrographs of a 0/90° lay down pattern (A) and detail of a strut intersection (B). (C) Photo of a tympanic membrane design. SEM micrographs of stacked fibers with 50 layers (35.7 ± 4.7 μm) (D), 100 layers (140.5 ± 8.9 μm) (E), and 200 layers (190.8 ± 20.8 μm) (F). Scale bars: A, 1 mm; B, 100 μm; C, 1 cm; and D−F, 100 μm.

corresponding optimal voltages of ≤8 kV. Flow rates between 0.08 and 0.3 mL/h were necessary, and the scan speeds had to be kept above 5 mm/s. The optimal temperature was kept at ∼20 °C and relative humidity ranged from 40 ± 2%.

2.7. Pattern Fabrication. Having established the optimal parameters of DW ESP for PEOT/PBT, we proceeded to design scaffolds (Video S1, SI). The design of a scaffold, such as its architecture and pore network, determines its success in a targeted TE application. While the architecture may guide and influence cartilaginous tissue formation,[31] porosity is essential not only for nutrient diffusion and waste removal,[2,23] but also allows and impacts cartilage ECM formation.[32,33] Conventional ESP processes lack on-demand patterning ability and typically produce compact meshes that hinder cell infiltration and ECM formation throughout their volume.[8]

DW ESP permits the tailored patterning of 3D ultrathin scaffolds with multiscale and controllable porosity, with a setup that dispenses any complex add-ins. Applying the optimized DW ESP parameters (Table S7, SI), we fabricated regular structures with a 0/90° lay down pattern (Figure 3A,B). The accuracy of this process also allowed the design and fabrication of more complex structures, such as one that mimics the anatomy of a tympanic membrane (Figure 3C). By tuning the distance between struts and the number of deposited layers, the pore size and scaffold thickness could be controlled. True 3D structures could be built, where 0/90° scaffolds with an approximate fiber spacing of 800 μm were fabricated with varying thickness based on the number of deposited layers: 35.7 ± 4.7 μm with 50 layers (Figure 3D), 140.5 ± 8.9 μm with 100 layers (Figure 3E), and 190.8 ± 20.8 μm with 200 layers (Figure 3F). The fabrication of scaffolds in the centimeter thickness range was hindered by the loss of the macroporous structure. As fibers were stacked, both the height and the width of the line pattern increased. This is attributed to a higher concentration of fibers on a single spot and, consequently, the accumulation of repulsive charges, leading to dispersion during the deposition process.[34]

To circumvent this issue, some strategies can be implemented. A stepwise approach of the layer-by-layer deposition could provide enough time for the dissipation of the residual charges, hence reducing the repulsive effect and yielding a more focused deposition. However, if the ESP process is interrupted between the fabrication of layers, multiple jet ejections are required. This is a limiting factor, since minor deviations can occur from the focusing spot, causing a mismatch between the deposited layers. However, if the ESP process is continued, the ejection time will be greatly enhanced and further jet instabilities may arise. Another strategy could be the hybridization of this system with a mechanism for charge compensation used in other applications, such as scanning electron microscopy.[35,36] Ji et al. reported a noticeable charge decrease on Al_2O_3 samples by employing an oxygen atmosphere through a local oxygen pressure device.[36] Finally, another possible solution is to invert the electrode polarity between layer depositions. In such a setup, the residual charges on the deposited fibers would be the opposite of the charges from the upcoming fibers, thus resulting in an attractive effect. Xu et al. followed this strategy and reported an increase in nanofiber deposition accuracy in a near-field ESP device.[34]

2.8. DW ESP with Other Polymers. In order to prove the versatility of this technique, we applied the same principle to a PCL solution and demonstrate a similar outcome (Figure S6, SI). We chose PCL due to its wide applications in the TE field. We kept the same solvents and used the ratio derived from the PEOT/PBT optimal solution, which yielded a fast evaporation rate, critical to collect the fibers in a dry state, as aforementioned. A polymer concentration of 20% (w/v) was found to be optimal, due to its fairly high viscosity, necessary to this process, while still flowing through the tubing and spinneret. We measured and compared the dynamic viscosity of PCL and PEOT/PBT solutions (Figure S6E, SI) and noticed a similar, yet slightly higher, value for the PCL solution. As for the ESP parameters, we used the same empirical evidence to define the DW window. Similarly, we observed a transition of the bundle morphology with different processing parameters. With an increase of the voltage, more-disperse fibers were produced, thus affecting the fiber bundle formation (Figure S6A−C, SI). For the latter morphology, we could see once

DOI: 10.1021/acsami.7b07151
ACS Appl. Mater. Interfaces 2017, 9, 38187−38200

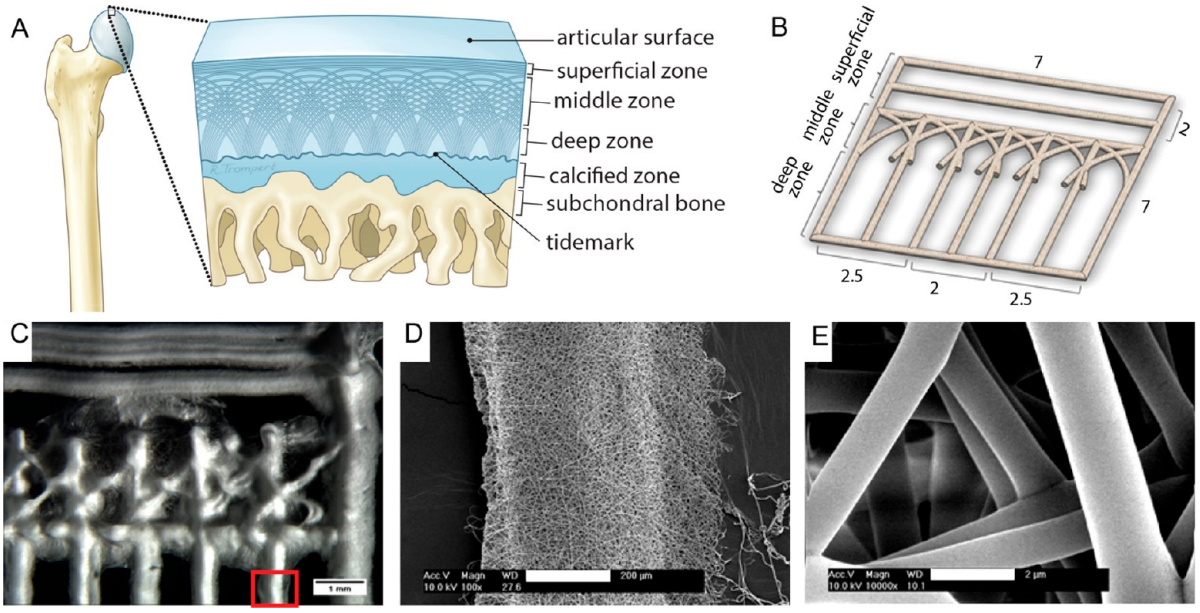

Figure 4. Design of an articular cartilage mimetic scaffold. (A) Illustration of the zonal configuration in native cartilage (2−4 mm thick). (B) 3D model representing the fabricated scaffold. Four of these scaffolds were stacked to form the final construct (dimensions are in millimeters). (C) Stereomicroscope image of the DW ESP structure, depicting the three different zones. (D) SEM micrograph showing a magnified view of the red rectangle marked in part C. (E) Detailed view of the individual fibers composing the scaffold (panel D). Scale bars: C, 1 mm; D, 200 μm; and E, 2 μm.

again that the bundle was composed of ultrathin fibers with a diameter of 1.42 ± 0.09 μm (Figure S6D, SI).

Differences in the ESP parameters and outcome can be explained by the inherent properties of both solutions. While some properties, such as surface tension and conductivity, can be better approximated by using the same solvents, polymer-derived properties, such as molecular weight of the polymer chains and their entanglement, will most likely differ when testing completely different materials. We postulated that the molecular weight of our PEOT/PBT formulation (M_n = 50 670)[37] and the resulting chain entanglement are decisive in maintaining the jet stability by balancing the repulsive forces through material cohesion. Therefore, we used a formulation of PCL with a M_n of 80 000, which was thought to provide a similar effect. In fact, due to a higher M_n and solution viscosity, the material cohesion of this PCL solution seems slightly higher, which explains the necessity to use higher voltages in order to obtain fully dispersed fibers (Figure S6C, SI). In summary, we have shown that our approach works in disparate materials and that there is a moderate discrepancy of solution properties for which similar results can be obtained, provided that the right ESP parameters are met.

2.9. Cell Seeding and Proliferation on DW ESP Scaffolds. Electrospun meshes generally facilitate cell attachment and distribution due to their ECM resemblance.[3] To determine whether our DW ESP scaffolds supported cell seeding and proliferation, we fabricated scaffolds with a fiber spacing of 860 μm and an average line width of 150 μm, and then seeded them with hMSCs (Figure S7C, SI). For comparison, we fabricated scaffolds with similar dimensions by AM (Figure S7B, SI). Seeding efficiency was evaluated by DNA quantification 1 day postseeding (Figure S7A, SI) and revealed that DW ESP scaffolds promoted 7 times more cell retention than those fabricated by AM techniques (17.66 ± 3.82% v. 2.43 ± 0.28%). To assess cell distribution and proliferation, the scaffolds were stained with methylene blue after 1 and 4 days of culture (Figure S8, SI). At day 1, cells seeded on the AM scaffolds were mostly retained at the fiber intersections (Figure S8A, SI), while those seeded on the DW ESP scaffolds were more abundant and well distributed (Figure S8C, SI). At day 4, both scaffolds supported cell proliferation, but a larger population was present on the DW ESP structure (Figure S8B,D, SI). These data argue that the DW ESP scaffolds promoted better cell seeding and retention compared to the AM scaffolds.

2.10. Fabrication of an Articular Cartilage Mimetic Scaffold. Having established that DW ESP could be used to fabricate scaffolds that support cell seeding and proliferation, we then tested whether this novel technique could be used to create a scaffold that mimics articular cartilage with its distinct multizone morphology (Figure 4A); such a scaffold may offer a superior template for in vitro cartilage formation and ECM organization.[38] We fabricated a scaffold that recapitulates three of the four main zones of cartilage (Figure 4B−E). The superficial zone, denoted by tangentially oriented collagen fibrils, was represented by two parallel electrospun layers with an average distance of 238 ± 79.3 μm. To reproduce the oblique collagen structure of the middle zone, we created crossed diagonal layers. Finally, the deep zone was represented by parallel layers, radially oriented to the top structure, with an average distance of 523 ± 156 μm. The mimetic scaffolds had pore dimensions that ranged from 238 ± 79 to 524 ± 156 μm, of which the values were within the ideal dimensions (250−500 μm) reported for chondrocyte proliferation and ECM secretion on gelatin scaffolds.[39] Detailed views of the fiber bundle and individual ultrathin fibers with an average diameter of 1.4 ± 0.6 μm (Figure S9, SI) are shown in parts D and E of Figure 4, respectively.

Next, we further characterized the mimetic scaffold's physical and mechanical properties (Table S6, SI). Overall, the measured porosity was 91.2 ± 1.0% (Table S6, SI). Tanaka et al. demonstrated that scaffolds with a porosity of 95% and

DOI: 10.1021/acsami.7b07151
ACS Appl. Mater. Interfaces 2017, 9, 38187−38200

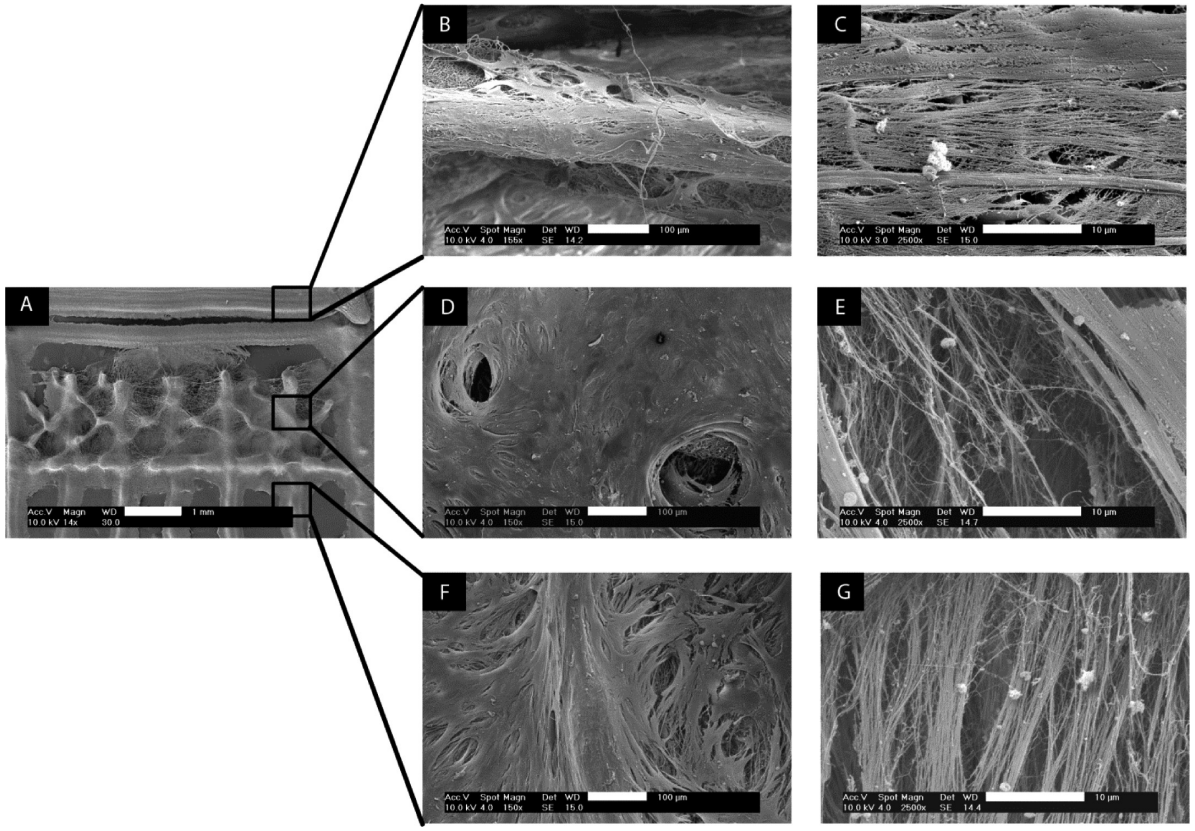

Figure 5. SEM images showing the topographical influence of the scaffold's architecture on tissue development (B, D, F) and matrix orientation (C, E, G) after 21 days of culture in chondrogenic medium. (A) Empty scaffold fabricated by DW ESP. Low-magnification images (B, D, F) and high-magnification images (C, E, G) of the superficial zone (B–C), middle zone (D–E), and deep zone (F–G). Scale bars: B, D, and F, 100 μm; C, E, and G, 10 μm.

pore size of 0.3 mm yielded the best cartilage regeneration among scaffolds with various kinds of porosity (80–95%) and pore sizes (0.3–2.0 mm).[40] However, such a high porosity is not univocal in regenerative articular cartilage. Our previous studies have demonstrated that pore size and shape are more important than total porosity in regenerating articular cartilage.[31,32] The mechanical properties of the scaffolds in dry condition were also characterized using a nanoindenter. Since the specific PEOT/PBT copolymer used has minimal swelling (below 5%), wet conditions were not deemed necessary for mechanical tests.[41] The measured Young's modulus in compression was 2.65 ± 0.65 MPa, which proved to be higher than human native cartilage as measured by in situ biphasic creep indentation (0.45 to 0.80 MPa) or bovine cartilage (0.08 to 2.1 MPa) measured by nanoindentation.[42−44]

In order to engineer a larger tissue construct, four individual scaffolds (each approximately 208.5 ± 19.4 μm thick) were stacked and bonded to yield an assembled structure of 1.39 ± 0.6 mm in height. The introduction of sacrificial layers of PEO between the spun mats promoted space between individual scaffold layers in the longitudinal direction, and the bonding process did not affect the inner core of the scaffolds (data not shown).

2.11. Cell Culture and Chondrogenic Differentiation. To investigate the potential of designed scaffolds for articular cartilage regeneration, we cultured hMSCs on stacked DW ESP scaffolds (unless otherwise stated) in chondrogenic and basic medium (negative control medium). Although the stacked DW ESP scaffolds showed varied patterns in the three different zones, fibers were randomly oriented in the bundles comprising the articular cartilage mimicking structures. Thus, we choose cell-seeded random fiber (RF) scaffolds as a control instead of aligned fiber scaffolds. For comparison, the fiber dimension and porosity of RF scaffolds were tailored to be similar to that of DW scaffolds. The cell proliferation on the DW and RF seeded scaffolds was evaluated at three time points during the first week of culture, using a PrestoBlue assay (Figure S10, SI). Proliferation was registered in all the conditions through an increase in the fluorescent signal. In both media, DW scaffolds showed 4-fold higher intensity compared to RF scaffolds, until day 7 when cell proliferation increased steeply on RF sheets. This observation can be explained by the higher number of fibers in the vicinity of cells, due to the lack of large pores on the RF structure, which leads to easier cell spreading, and thus a faster proliferation rate. For chondrogenic differentiation, cells on DW scaffolds showed a steady increase in fluorescence over the 7 days. In contrast, the signal from cells incubated on RF scaffolds in differentiation medium showed little change over the same period. These data indicate that cells proliferated on both RF and DW scaffolds.

To determine the topographical influence of DW mimetic scaffolds on tissue development and matrix secretion, scanning electron microscopy (SEM) observations were performed after 21 days of culture in chondrogenic medium. Whereas the RF and DW scaffolds both demonstrated full coverage of cells, only the DW scaffolds showed cells and matrix throughout their volume (Figure S11, SI).

DOI: 10.1021/acsami.7b07151
ACS Appl. Mater. Interfaces 2017, 9, 38187−38200

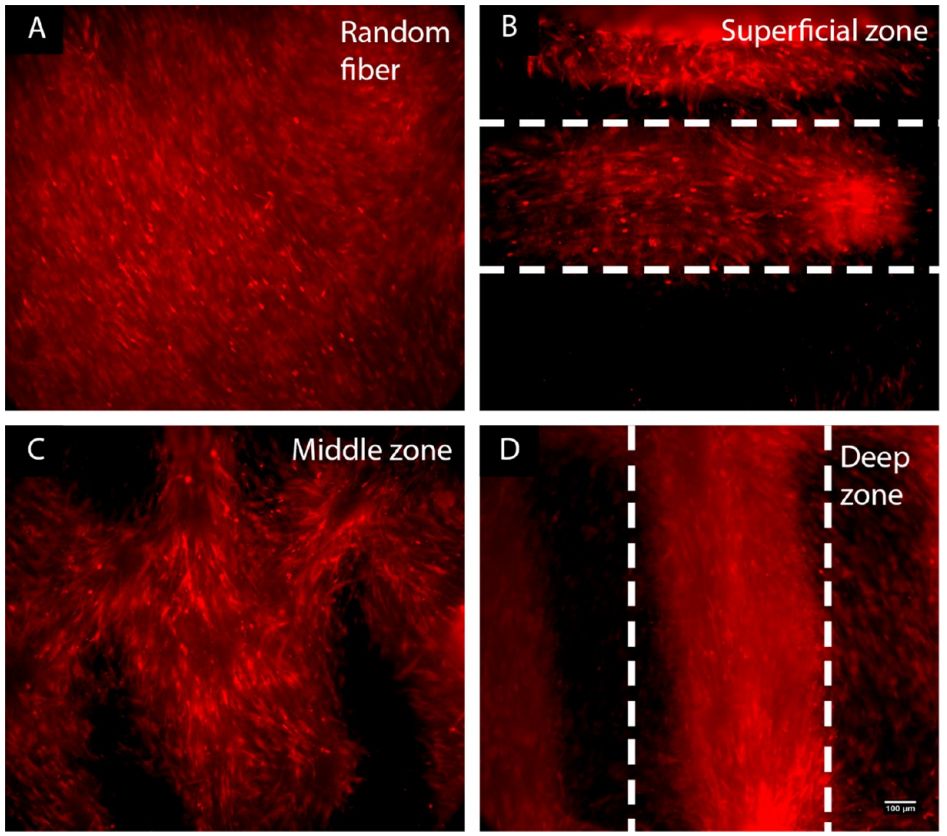

Figure 6. Immunostaining of collagen type I on hMSCs seeded scaffolds after 21 days of culture in chondrogenic medium: (A) RF scaffolds and (B–D) sections of the DW scaffolds, as labeled. The scale bar in D (100 μm) applies to all panels. The dashed lines in panels B and D delineate the collagen fiber orientation.

When cultured on the RF meshes, hMSCs dispersed randomly. As a consequence, their secreted matrix was isotropically distributed (data not shown). In contrast, the matrix organization was influenced by the zonal topography of the DW scaffolds (Figure 5). The horizontal layers forming the superficial zone (Figure 5C) and the vertical layers of the deep zone (Figure 5G) promoted tissue development along their respective axes, which resulted in the anisotropic formation of fibrils. Coherence analysis of the SEM micrographs showed a slightly higher coefficient of directionality for the deep zone (0.49 ± 0.08) compared to the superficial zone (0.41 ± 0.09) (Figure S12, SI).

The oblique layers that represent the middle zone induced tissue formation in a more random manner, with secreted fibers displaying a crossed pattern (Figure 5E). The coefficient of directionality for this middle zone was 0.33 ± 0.11 (Figure S12, SI). The presence of holes (Figure 5D) suggested the formation of tissue in different and opposite directions. In summary, the DW scaffold imparted a tissue and matrix organization in a zone-dependent way, in contrast to the isotropy seen in the RF sheets.

The morphology and feature size of the fibrils observed in the SEM micrographs suggested the presence of collagen. Among collagen types, type II collagen is the basis for articular cartilage. To investigate the formation of collage type II, the surface of the scaffolds was immunostained against collagen type II after 21 days of culture in chondrogenic medium, but no signal was detected. hMSC pellets after 21 days in chondrogenic medium showed collagen type II staining (Figure S13C–F, SI), suggesting that pellet conditions (such as greater cell–cell contact, maintenance of cell rounded shape, softer substrate, and reduced oxygen tension) resulted in improved differentiation of hMSCs and consequent production of collagen type II.[45−47] We are investigating whether modifications to the cell culture conditions that provide an environment more similar to the pellet conditions, such as using a hydrogel for scaffold coating or a cell carrier like hyaluronic acid (Figure S14, SI), will improve chondrogenic differentiation and collagen I and II production. When cultured on flat substrates, differentiated chondrocytes might dedifferentiate into fibroblast-like cells and produce collagen type I instead.[48] Therefore, we further immunostained the scaffolds for collagen type I (Figure 6). We observed distinct collagen type I staining that resembled the matrix patterning. The RF scaffolds revealed random, nonpreferential direction of collagen type I staining (Figure 6A). For the DW scaffolds, collagen type I anisotropy was observed for the top (Figure 6B) and bottom layers (Figure 6D), and an arclike configuration was seen for the middle layer (Figure 6C). These results indicate that the DW scaffolds enabled collagen matrix organization in a zone-dependent way, in contrast to the isotropy seen in the RF meshes.

To determine whether the observed patterns in SEM were cartilage-specific matrix, we visualized sulfated glycosaminoglycan (GAG) by staining the scaffolds with Alcian Blue after 21 days of culture. Cultured cell pellets were also stained as a positive control (Figure S13A,B, SI). As shown in Figure S15 (SI), both RF and DW scaffolds present higher amount of GAG staining in chondrogenic medium compared to basic medium (control medium). In chondrogenic medium, GAG staining

DOI: 10.1021/acsami.7b07151
ACS Appl. Mater. Interfaces 2017, 9, 38187−38200

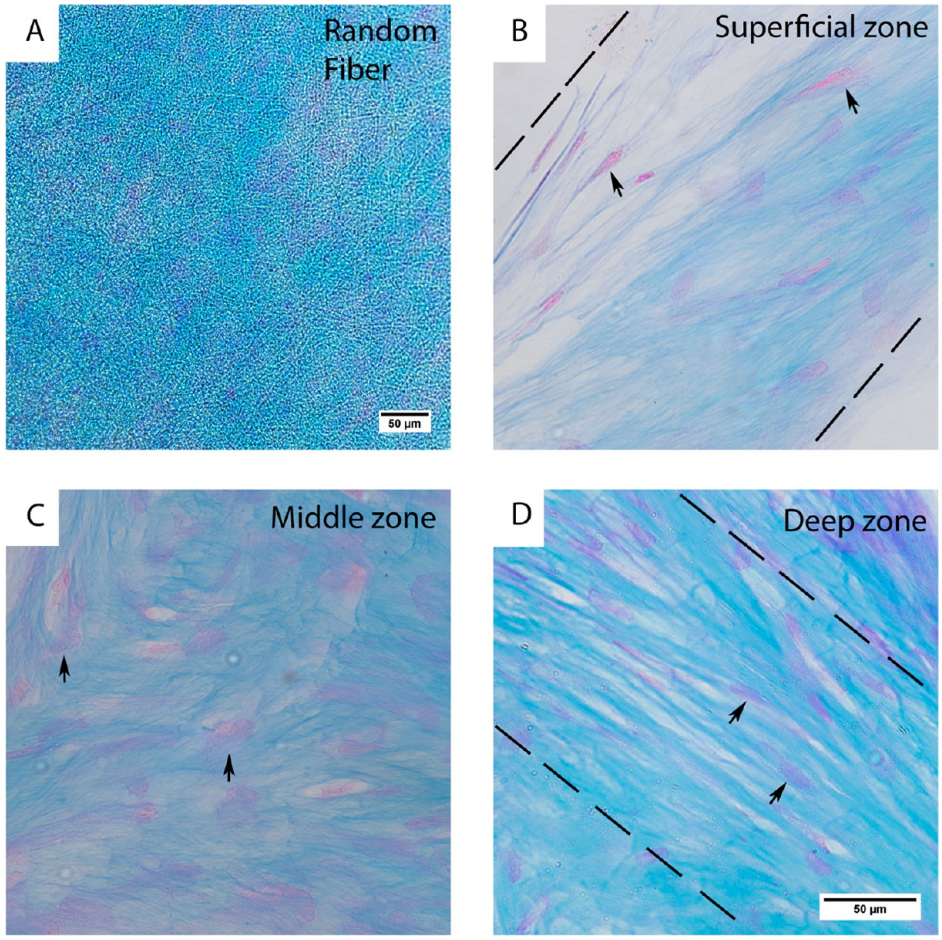

Figure 7. Staining with Alcian Blue for sulfated GAGs and Nuclear Fast Red for cell nuclei in histological sections of hMSCs after 21 days of culture in chondrogenic medium on RF (A) and DW (B–D) scaffolds. (A) A 10× view of the RF scaffold. A 20× view of the top (B), middle (C), and bottom (D) sections of DW ESP scaffolds. The dashed lines represent the direction on the layer (parallel to its axis) and the arrows point to cells. The scale bar in D also applies to panels B and C.

was abundant and distributed all over the RF scaffold (Figure 7A). For the DW scaffolds, we observed GAG staining in a zonal distribution and distinct cell morphology (Figure 7B–D). For the top (Figure 7B) and bottom (Figure 7D) layers of the scaffolds, we observed anisotropic GAG staining and cell elongation along the same direction. This was particularly evident in the top layer, with the presence of some flattened cells on the most superficial zones, which resembled the native state. GAG staining was more randomly dispersed in multiple directions for the middle section (Figure 7C), and the cells were more rounded compared with the other scaffold zones.

Quantification of GAG production showed similar levels for both scaffolds (Figure 8A). However, cell adhesion and proliferation were significantly greater in DW scaffolds compared to RF sheets (Figure 8B). As a consequence, the RF sheets exhibited significantly higher GAG/DNA ratios (Figure 8C), or more matrix production normalized to cell content, compared to DW scaffolds. Although seeded at the same density (per volume), RF sheets may achieve cell confluency at an earlier time compared to DW scaffolds due to their smaller available growth area. Therefore, cells grown on RF scaffolds were subjected to higher cell–cell interaction throughout the culture period. Reports in the literature show that higher cell densities, as a consequence of higher cell–cell interaction, enhance matrix production in cultures with hMSCs[49] and articular chondrocytes,[50] which could explain our observed differences. Quantification of GAG and DNA levels after cells achieve full confluency on the scaffolds may help clarify this difference.

Finally, the cell-seeded scaffolds were examined for the presence of several chondrogenic markers, including collagen type II alpha 1 (Col2a), Sox9, and aggrecan (ACAN). Col2a and ACAN are major proteins found in cartilage matrix.[51,52] Sox9 is a transcription factor that plays a key role in chondrogenes.[53,54] The cell-seeded scaffolds cultured in basic medium were used as control. Levels of mRNA for all three markers were higher for DW scaffolds in chondrogenic medium compared to basic medium (Figure 8D–F). In chondrogenic medium, expression of Sox9 and ACAN was significantly higher in DW scaffolds compared to RF scaffolds after both 14 and 21 days of culture (Figure 8E,F). Cellular aggregation or mesenchymal condensation is essential for the process of chondrogenesis.[55] The surface topography of scaffolds, including patterns and pore size, was already shown to have an influence on cellular aggregation.[55–57] In the present work, the upregulation of Sox9 and ACAN on DW scaffolds could be ascribed to the distinct surface patterns and pore size of DW scaffolds, which provided a better 3D environment for cellular organization and compactness. However, the higher expression of Sox9 and ACAN did not always result in a higher expression of Col2a. Col2a expression was higher for the RF scaffolds compared to the DW scaffolds at day 21 in chondrogenic

DOI: 10.1021/acsami.7b07151
ACS Appl. Mater. Interfaces 2017, 9, 38187–38200

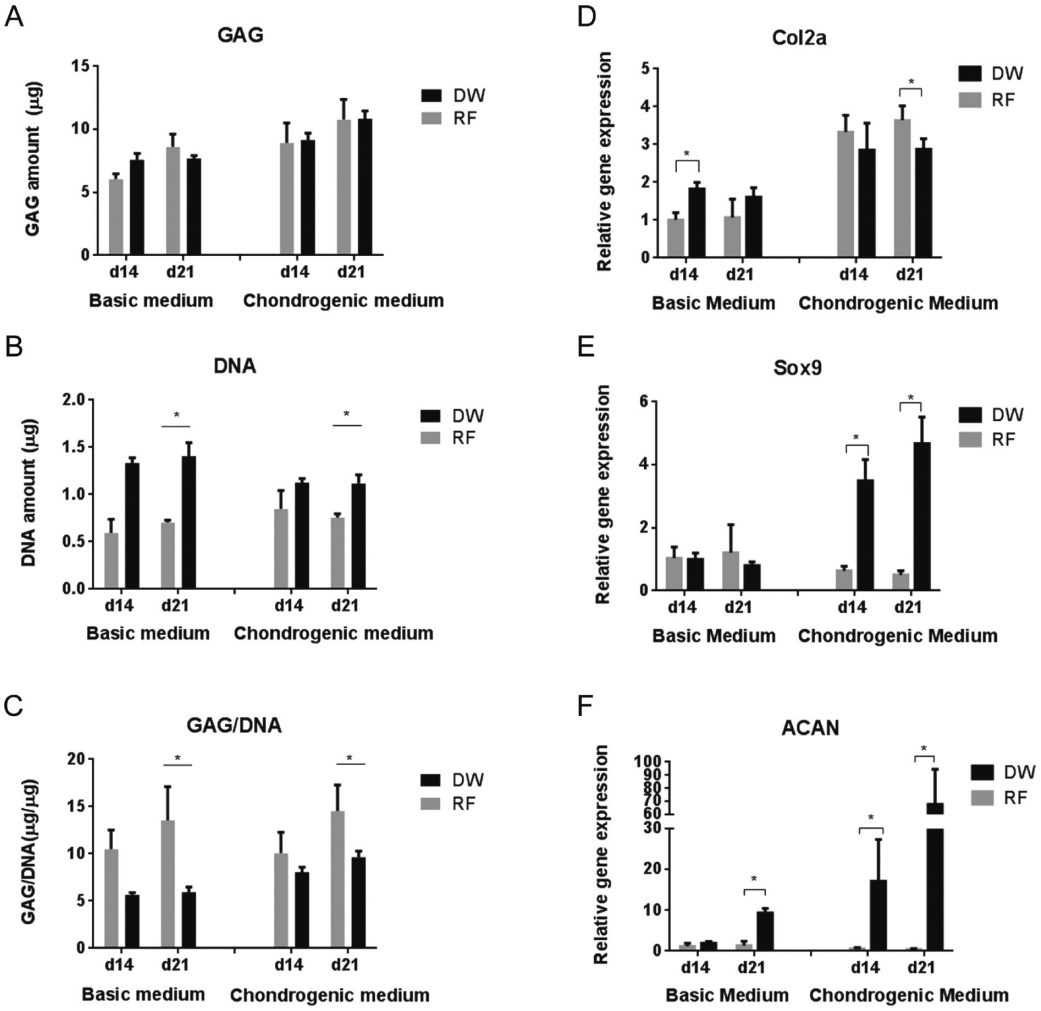

Figure 8. Cartilaginous matrix production (A–C) and gene expression profiles (D–F) of hMSCs cultured for 14 and 21 days in basic and chondrogenic medium. (A) Total GAG amount, (B) total DNA amount, and (C) GAG normalized to the DNA content. mRNA levels of Col2A (D), Sox9 (E), and ACAN (F) are represented as fold differences relative to the expression obtained in RF samples cultured in basic medium at day 14. *$p < 0.05$.

medium (Figure 8D). This uncoupling of Col2a and Sox9 expression was also reported by Aigner et al., who demonstrated that Sox9 was not the central regulatory mediator of Col2a in human articular chondrocytes.[58] They demonstrated that high gene expression of Sox9 did not lead to an increase of Col2a expression in normal articular chondrocytes and that the amount of Col2a expression was higher in spite of reducing Sox9 expression in osteoarthritic chondrocytes. The higher expression of Sox9 in DW scaffolds could be responsible for the higher expression of ACAN in DW scaffolds. Previous studies demonstrated that Sox9 supported the aggrecan promoter activity in clonal chondrocytic cells.[54] These data argue that DW scaffolds supported early chondrogenic differentiation of hMSCs.

3. CONCLUSION

We have shown here the development of a technique for direct writing with electrospinning, with the capability to control the fiber bundle morphology and to fabricate regular 3D ultrathin structures, applicable to different materials. Applying this technique, we produced a scaffold that mimics the zonal organization of articular cartilage and compared its performance for cartilage tissue formation to a regular electrospun sheet. In contrast to nonspecific deposition by the typical electrospun meshes, DW scaffolds were able to direct tissue organization and fibril matrix orientation. Expressions of chondrogenic markers, including Sox9 and ACAN, were also significantly enhanced in this structure. Our work provides a new technique for the patterning of nano/microfibrous structures with potentially wide application for the engineering of many tissues, particularly those presenting regional differences. Further optimization might enable the fabrication of articular cartilage suitable for therapeutic applications.

4. MATERIALS AND METHODS

4.1. Polymer Solution Preparation. A polyethylene terephthalate/polybutylene terephthalate (PEOT/PBT) block copolymer (PolyVation B.V.; the weight ratio of PEOT/PBT = 55/45, and the molecular weight (g/mol) of the starting PEG segments used in the polymerization process is 300) was dissolved in a mixture of chloroform ($CHCl_3$, Sigma-Aldrich) and 1,1,1,3,3,3-hexafluoro-2-propanol (HFIP, Biosolve-Chemicals) to prepare the polymer solutions. Solutions of 26–30% of polymer (w/v) in 70:30 to 80:20 $CHCl_3$/HFIP (v/v) were formulated. Polycaprolactone (PCL, M_n = 80 000, Sigma-Aldrich) solutions were prepared with 20% (w/v) in 75:25 $CHCl_3$/HFIP.

DOI: 10.1021/acsami.7b07151
ACS Appl. Mater. Interfaces 2017, 9, 38187–38200

4.2. Electrospinning Setup. The ESP system configuration consisted of a two parallel plate setup, composed of a top unit (21.5 × 30 cm) of a 2 cm thick copper plate encased in Teflon and a 0.5 cm thick copper collector (10 × 10 cm) mounted on an *XY* translational stage. The stage is a modified 3D printer (k8200, Velleman), specifically customized for ESP experiments and controllable using Repetier-Host software (v0.84, Repetier).

4.3. Electrospinning Tests and Jet Imaging. Initial electrospinning experiments to assess the drawing region were carried out with polymer solutions of 26−30% PEOT/PBT in 70:30 to 80:20 $CHCl_3$/HFIP (v/v). The applied voltage was varied from 2.0 to 16 kV and the working distance from 2 to 16 cm, the flow rate from 0.05 to 2 mL/h, the temperature from 18.5 to 30 °C, and the relative humidity from 25% to 55%. The scan speed was varied from 1 to 13 mm/s and the spinneret diameter was fixed to 0.5 mm. After jet initiation, the collector was set to a linear motion to collect the fibers in a single direction. A gross visual examination of the outcome and scanning electron microscope (SEM) analysis were done to analyze the contribution of each parameter to the jet stability and to define the parameters range for drawing capability.

ESP tests within the drawing region were carried with a 28% PEOT/PBT in 75:25 $CHCl_3$/HFIP (v/v). The applied voltage varied from 4 to 8 kV, the working distance from 2 to 7 cm, and the scan speed from 1 to 13 mm/s. The flow rate was set to 0.18 mL/h through a spinneret with 0.8 mm diameter. A temperature of 20 °C and a relative humidity of 30% were used as ambient parameters. SEM micrographs were then taken to investigate the fiber bundle morphology within the drawing region.

ESP tests with PCL solutions were carried out using the same approach but different settings. The voltage was varied from 7 to 16 kV and the working distance from 3 to 6 cm, and the scan speed was set at 10 mm/s. The flow rate was tested between 1 and 5 mL/h through a 0.5 mm spinneret. The temperature was established at 21−23 °C and the relative humidity between 35% and 45%.

Images of the jet flight were captured using a digital camera (Panasonic Lumix DMC G3) and the resulting photographs were further treated with ImageJ.

4.4. Direct Writing and Scaffold Fabrication. Direct writing experiments and scaffold fabrication were carried with a polymer solution of 28% PEOT/PBT in 75:25 $CHCl_3$/HFIP (v/v) with the experimental parameters listed in Table S7 (SI). For the fabrication of the assembled scaffolds, the electrospun mats were stacked via a manual process illustrated in Figure S16 (SI). Briefly, the scaffolds were detached from the aluminum foil by placing them in deionized (DI) water for 1−2 min and gently tapping the structure with tweezers to promote detachment. After drying with filter paper, the scaffolds were placed on top of a polydimethylsiloxane (PDMS) block covered with a Teflon sheet and held in place with thin metal wires. Overall, four scaffolds were stacked together to achieve the final constructs. To promote the space between individual scaffold layers, a thin poly(ethylene oxide) (PEO, M_w = 900 000 g/mol, Sigma-Aldrich) sheet (300 μm thick) fabricated through solvent casting of 3% PEO in 80:20 H_2O/ethanol (v/v) was placed between each scaffold. The stacked layers were then bound together by joining the vertexes of each scaffold and melting them at 180 °C (using a micro-soldering iron). After that, the thin metal wires were removed from the scaffolds. The assembled constructs were then placed overnight in a container filled with DI water under agitation to dissolve the sacrificial PEO layers. Following this process, the scaffolds were retrieved and allowed to dry.

The fabrication of random fiber (RF) sheets was carried out using the same polymer solution and setup, with the process parameters listed in Table S7 (SI), which were selected to fabricate a mesh with similar fiber dimensions as the DW scaffolds. The collector was set to a raster scan path with a step size on the *Y* axis of 1 mm to ensure thickness uniformity on the deposited meshes. Scaffolds with a diameter of 12 mm were then punched out for further cell culture study.

4.5. Scaffold Characterization. The scaffold geometry and architecture was characterized through measurements on SEM micrographs. The height of the final assembled construct was measured using a digital caliper. The porosity of the electrospun scaffold was calculated using the theoretical approach described in eq 1

$$\text{porosity}\ (\%) = \left(1 - \frac{m_{\text{scaffold}}}{\rho_{\text{material}} V_{\text{scaffold}}}\right) \times 100\% \quad (1)$$

where m_{scaffold} is the measured weight of the scaffold, ρ_{material} is the density of the material (1.2 g/mL),[59] and V_{scaffold} is the apparent volume of the scaffold (assuming a solid block of equal dimensions). To determine the Young's modulus under compression of the electrospun scaffolds, a mechanical test was performed using a nanoindentation device (Piuma, Optics 11). The compression test on the scaffold was carried out with a tip radius (r) of 22.5 μm and spring constant (k) of 78.3 N/m. Forty indentations were performed with a step size of 50 μm on the *X* axis and 5 μm on the *Y* axis.

4.6. Cell Culture. Preselected hMSCs (male age 22) were retrieved from the Institute of Regenerative Medicine at Texas A&M University.[60,61] Briefly, a bone marrow aspirate was drawn from the patient after informed written consent, and mononuclear cells were separated using density centrifugation. hMSCs at passage 2 were expanded in basic medium (BM) composed of α-MEM (Thermo Fisher Scientific) supplemented with 10% fetal bovine serum (Lonza), 2 mM L-glutamin (Thermo Fisher Scientific), 0.2 mM ascorbic acid (Sigma-Aldrich), and 100 units/mL penicillin plus 100 mg/mL streptomycin (Thermo Fisher Scientific) until reaching 80−85% confluence. The medium was refreshed every 2 days.

4.7. Pellet Culture. To check the donor potential for chondrogenesis, a pellet culture study was performed over 21 days as a positive control. About 2 × 10^5 cells suspended in 200 μL of chondrogenic medium composed of DMEM (Thermo Fisher Scientific) supplemented with 1% ITS premix (Micronic BV), 50 μg/mL ascorbic acid (Sigma-Aldrich), 40 μg/mL proline (Sigma-Aldrich), 100 μg/mL sodium pyruvate (Life Technologies), 100 units/mL penicillin plus 100 mg/mL streptomycin (Thermo Fisher Scientific), 0.01 μg/mL TGF-β3 (R&D systems), and 100 nM dexamethasone (Sigma-Aldrich) were seeded in a round-bottomed nontreated tissue culture 96-well plate. For pellet formation, the cells were centrifuged at 2000 rpm for 3 min at 4 °C. As a control the cells were seeded in BM using the same protocol. The medium was refreshed every 2 days, taking out 100 μL and adding 100 μL. The pellets were fixed in 4% paraformaldehyde for 2 h at 4 °C and then washed three times with phosphate-buffered saline solution (PBS) and maintained wet.

4.8. Seeding Efficiency and Proliferation on AM vs DW ESP Scaffolds. 3D scaffolds made of PEOT/PBT were fabricated via additive manufacturing (Bioscaffolder, SysENG).[32] hMSCs were seeded on DW ESP and AM scaffolds at a density of 5 × 10^4 cells/cm^2 and cultured in BM for 4 days, with medium changes every other day. Cell attachment was evaluated by DNA quantification using a CyQUANT Cell Proliferation Assay Kit (Thermo Fisher Scientific). Briefly, the scaffolds were washed three times with PBS, transferred to a 1.5 mL Eppendorf tubes, and placed at −80 °C overnight. After this, three freeze/thaw cycles (from −80 °C to room temperature) were applied, and 250 μL of proteinase K digestion buffer [0.001% (w/v) proteinase K, 10% of 1.85 mg/mL iodoacetamide (Sigma-Aldrich) solution, and 10% of 100 μg/mL pepstatin A (Sigma-Aldrich) solution in Tris/EDTA buffer] was added to every tube, followed by incubation at 56 °C for 16 h under agitation. The lysate was collected and used to measure the DNA amount in the scaffolds using the kit protocol. Cell distribution and proliferation were assessed with Methylene Blue staining. Briefly, samples were fixed in 10% formalin solution for 30 min, followed by a rinse with demineralized water for 1 min. After that, samples were put in 1% Methylene Blue solution for 60 s and washed with demineralized water again three times. Images were acquired with a stereomicroscope (SMZ25, Nikon).

4.9. Cell Seeding and Culture on RF Sheets and DW ESP Scaffolds. Prior to cell seeding, samples were placed in a nontreated tissue culture 24-well plate (O-rings were used to prevent the scaffolds from floating), sterilized in 70% ethanol for 1 h, and washed three times with PBS. After removing the PBS, the scaffolds were prewetted

DOI: 10.1021/acsami.7b07151
ACS Appl. Mater. Interfaces 2017, 9, 38187−38200

in BM overnight for the next step of cell seeding. Cells were seeded on each scaffold at a similar density (12 000 cells/mg of material) unless otherwise stated. After cell attachment, a final volume of 1 mL of CM was applied for each well. Cell culture on scaffolds in BM was used as the negative control. Cell culture on scaffolds was kept for 21 days and the medium refreshed every 2−3 days.

4.10. Scanning Electron Microscopy (SEM) Analysis. The cell-seeded scaffolds (n = 4) were washed three times with PBS, fixed during 2 h in 10% neutral buffered formalin, washed again three times with PBS, dehydrated in a series of ethanol dilutions (1 × 50, 60, 70, 80, 90, and 96% and 2 × 100%) for 30 min and then critical point dried with liquid carbon dioxide (Balzers CPD 030 and Leica EM CPD 300). Following this, samples were gold-sputtered (Cressington Sputter Coater 108 auto) for 40 s at 30 mA and then imaged using a SEM (Philips XL-30 ESEM, Philips, and Versa 3D, FEI) at V = 10 kV. For analysis of the fiber diameter and morphology and characterization of the electrospun scaffolds, the samples were gold-sputtered and imaged using the same parameters.

4.11. Metabolic Activity. The cell metabolic activity was measured at days 1, 4, and 7 using the PrestoBlue Cell Viability Reagent (Life Technologies). Briefly, a 10% (v/v) prestoBlue solution in culture medium was added to each sample (n = 4), which was incubated at 37 °C, 5% CO_2 during 2 h, protected from light. After that time, 150 μL aliquots were transferred to a black 96-well plate, and the fluorescence was measured in a PerkinElmer Victor3 plate reader (PerkinElmer) using the following parameters for excitation/emission: 560/590 nm. Blanks of medium only were made to correct for background fluorescence.

4.12. Real-Time Quantitative Polymerase Chain Reaction (qPCR). Gene expression of the chondrogenic markers including Col2a, Sox9, and ACAN was evaluated after 14 and 21 days of culture. Total RNA was isolated from the samples using a TRIzol-based extraction method followed by the Isolate II RNA Mini Kit (Bioline). Briefly, 1 mL of TRIzol reagent (Thermo Fisher Scientific) was added to each sample, followed by centrifugation at 12 000 rcf for 2 min at 4 °C, addition of 0.2 mL of a $CHCl_3$:isoamyl alcohol mixture, and again centrifugation at 12 000 rcf for 15 min at 4 °C. The aqueous phase was then collected and the rest of the procedure was conducted using the Isolate II RNA Mini kit protocol. RNA quantification and purity assessment were done in a NanoDrop 2000 (Thermo Fisher Scientific). cDNA was synthesized using the SensiFAST cDNA Synthesis Kit (Bioline) according to the manufacturer's protocol. qPCR was performed in the CFX Connect Real-Time PCR Detection System (Bio-Rad) using the SensiMix SYBR & Fluorescein Kit (Bioline) and the primers listed in Table S8 (SI). Twenty-five microliters of sample volume composed of 3 μL of cDNA, 12.5 μL of kit reagent, 7.5 μL of distilled water, and 1 μL of forward and reverse primer was used in the amplification process. For this, cDNA was first denatured for 10 min at 95 °C, followed by 45 cycles, consisting of 15 s at 95 °C, 15 s at 60 °C, and 15 s at 72 °C. Ct values were determined and normalized to the housekeeping gene B2M, and ΔCt = (average of $Ct_{control}$) − (Ct_{value}). The relative mRNA of the markers of interest is represented as fold changes relative to the expression obtained in the random fiber samples cultured in basic medium and calculated by $2^{-\Delta\Delta Ct}$.

4.13. Immunohistochemistry. Samples (n = 3) were retrieved after 21 days of culture, washed three times with PBS, and fixed for 30 min in 4% paraformaldehyde, at 4 °C. Samples were permeabilized in 0.5% Triton X-100 for 5 min at room temperature, followed by incubation with blocking buffer (0.05% Tween 20, 5% goat serum, and 1% BSA in PBS) overnight. Afterward, a mouse monoclonal anticollagen type I (1:100; Thermo Fisher scientific) or a mouse monoclonal anticollagen type II (1:50; Novus Biologicals) was added, and samples were incubated overnight again at 4 °C. The following day, samples were washed three times with wash buffer (blocking buffer without goat serum) and incubated with goat anti-mouse Alexa Fluor 647 secondary antibody (Invitrogen) (1:300) in wash buffer for 1.5 h at room temperature. Cell nuclei were stained with DAPI (0.1 μg/mL in PBS) for 5 min, followed by washing in PBS (three times). Samples without primary antibodies were used as a negative control. Fluorescent images were acquired using an inverted fluorescent microscope (Nikon Eclipse Ti−S).

4.14. Glycosaminoglycan (GAG) Assay. GAG and DNA measurements were performed after 14 and 21 days of culture. Samples (n = 4) were washed with PBS, transferred to a 1.5 mL Eppendorf tube, and stored dry overnight at −80 °C. Three freeze/thaw cycles (from −80 °C to room temperature) were applied to all the samples, and 250 μL of proteinase K digestion buffer (the formulation as describe above) was added to each tube, followed by incubation at 56 °C for 16 h, under agitation. The lysate was collected and used to measure the GAG amount and respective DNA content. The GAG amount was determined spectrophotometrically after reaction of 25 μL of lysate mixed with 5 μL of NaCl solution (2.3 M) with 150 μL of dimethylmethylene blue dye (DMMB, Sigma-Aldrich). The intensity of color change was quantified immediately by measuring the absorbance at 525 nm in a microplate spectrophotometer (CLARIOstar, BMG Labtech). The GAG content was then calculated using a standard of chondroitin sulfate (Sigma-Aldrich). The DNA amount was determined following the protocol described above.

4.15. Histology. Pellets and cell-seeded scaffolds (n = 3) were retrieved after 21 days of culture, washed with PBS, and fixed overnight in 10% neutral buffered formalin, at 4 °C. Subsequently, samples were dehydrated through a graded ethanol series (1 × 50, 60, 70, 80, 90, and 96% and 2 × 100%), cleared with butanol (2 h), infiltrated with liquid paraffin (overnight), embedded in paraffin, and stored at −20 °C. Sections 10 μm in thickness were cut with a microtome (HM355S, Thermo Fisher Scientific), mounted in poly-L-lysine precoated slides, and stained with 0.5% (w/v) Alcian Blue solution in 1 M HCl (pH 1.0, Sigma-Aldrich) for sulfated GAG and with Nuclear Fast Red for cell visualization. Microphotographs were then acquired using an inverted fluorescent microscope (Nikon Eclipse Ti−S) equipped with a color camera (DS-Ri2).

4.16. Image Analysis. SEM images were analyzed for fiber alignment quantification using the ImageJ software. The plugin OrientationJ was employed for this purpose, and the images were analyzed over the same ROI. Measurements (n = 30) were performed per condition, and the results are expressed in terms of the directional coherency coefficient, on a scale from zero to one. A coherency coefficient close to one, represented as a slender ellipse, indicates a strongly coherent orientation of the local fibers in the direction of the ellipse long axis. A coherency coefficient close to zero, represented geometrically as a circle, denotes no preferential orientation of the fibers.[49]

4.17. Statistics. Statistical significance was assessed with an unpaired t test on the fiber diameter study. A p-value <0.05 was considered significant. For the biological study, statistical significance was assessed using nonparametric tests. For comparison between two groups, the Mann−Whitney U test was used, and for comparison between three groups, the Kruskal−Wallis test was applied. A p-value <0.05 was considered significant. All the values are expressed as the average ± standard deviation.

■ ASSOCIATED CONTENT

Supporting Information

The Supporting Information is available free of charge on the ACS Publications website at DOI: 10.1021/acsami.7b07151.

Video showing solution electrospinning in the direct writing approach (AVI)

Methods for polymer solution characterization, influence of processing parameters on the deposited line consistency, the morphology of the point pattern created by spinning at a single point for a prolonged period, the effect of spinning parameters on the fiber morphology, DW ESP with PCL, comparison of cell seeding efficiency between 3D printed scaffolds and DW ESP scaffolds, Methylene Blue staining on 3D-printed scaffolds and DW scaffolds, frequency distribution of individual fiber diameters from articular cartilage mimetic scaffolds,

DOI: 10.1021/acsami.7b07151
ACS Appl. Mater. Interfaces 2017, 9, 38187−38200

PrestoBlue measurements of cell-seeded DW and RF scaffolds, SEM micrographs of DW and RF cell-seeded scaffolds, directional coherency of fibril matrix in DW ESP scaffold, immunostaining and histological staining of hMSCs in pellet culture, scaffold embedding with a hyaluronic acid hydrogel, scaffold mounting process, Alcian Blue and Nuclear Fast Red staining of RF and DW ESP, comparison of current direct-writing ESP techniques, summary of the obtained fiber morphologies with varying working distances and voltages, processing parameters used for DW ESP of PEOT/PBT, fiber alignment as a function of voltage and working distance, characterization of the articular cartilage mimetic scaffold, list of ESP parameters used for pattern and scaffold fabrication, and a list of qPCR primers sequences (PDF)

AUTHOR INFORMATION

Corresponding Author

*E-mail: l.moroni@maastrichtuniversity.nl.

ORCID

Honglin Chen: 0000-0001-7423-342X

Author Contributions

†H.C. and A.d.B.F.B.M. contributed equally to this work.

Notes

The authors declare no competing financial interest.

ACKNOWLEDGMENTS

H.C. thanks the China Council Scholarship program for financial support (Grant # 2011614016). Some of the materials employed in this work were provided by the Texas A&M Health Science Center College of Medicine Institute for Regenerative Medicine at Scott & White through a grant from NCRR of the NIH (Grant # P40RR017447). This project has been made possible with the support of the Dutch province of Limburg.

REFERENCES

(1) Mota, C.; Puppi, D.; Chiellini, F.; Chiellini, E. Additive Manufacturing Techniques for the Production of Tissue Engineering Constructs. *J. Tissue Eng. Regener. Med.* **2015**, *9* (3), 174−190.

(2) Wang, X.; Ding, B.; Li, B. Biomimetic Electrospun Nanofibrous Structures for Tissue Engineering. *Mater. Today* **2013**, *16* (6), 229−241.

(3) Hutmacher, D.; Woodfield, T.; Dalton, P.; Lewis, J. Scaffold Design and Fabrication. In *Tissue Engineering*, 1st ed.; van Blitterswijk, C., Thomsen, P., Lindahl, A., Hubbell, J., Williams, F. D.; Cancedda, R., de Bruijn, J., Sohier, J., Eds.; Academic Press, 2008; Chapter 14, pp 403−454.

(4) Lee, J.; Jeong, Y. H.; Cho, D. W. Fabrication of Nanofibrous Mats with Uniform Thickness and Fiber Density. *Macromol. Mater. Eng.* **2014**, *299* (9), 1052−1061.

(5) Sun, B.; Long, Y.; Zhang, H.; Li, M.; Duvail, J.; Jiang, X.; Yin, H. Advances in Three-dimensional Nanofibrous Macrostructures via Electrospinning. *Prog. Polym. Sci.* **2014**, *39* (5), 862−890.

(6) Bhardwaj, N.; Kundu, S. C. Electrospinning: a Fascinating Fiber Fabrication Technique. *Biotechnol. Adv.* **2010**, *28* (3), 325−347.

(7) Rogers, C. M.; Morris, G. E.; Gould, T. W.; Bail, R.; Toumpaniari, S.; Harrington, H.; Dixon, J. E.; Shakesheff, K. M.; Segal, J.; Rose, F. R. A Novel Technique for the Production of Electrospun Scaffolds with Tailored Three-dimensional Micro-patterns Employing Additive Manufacturing. *Biofabrication* **2014**, *6* (3), 035003.

(8) Brown, T. D.; Dalton, P. D.; Hutmacher, D. W. Direct Writing by Way of Melt Electrospinning. *Adv. Mater.* **2011**, *23* (47), 5651−5657.

(9) Lee, J.; Lee, S. Y.; Jang, J.; Jeong, Y. H.; Cho, D.-W. Fabrication of Patterned Nanofibrous Mats using Direct-write Electrospinning. *Langmuir* **2012**, *28* (18), 7267−7275.

(10) Sun, D.; Chang, C.; Li, S.; Lin, L. Near-field Electrospinning. *Nano Lett.* **2006**, *6* (4), 839−842.

(11) Neubert, S.; Pliszka, D.; Góra, A.; Jaworek, A.; Wintermantel, E.; Ramakrishna, S. Focused Deposition of Electrospun Polymer Fibers. *J. Appl. Polym. Sci.* **2012**, *125* (1), 820−827.

(12) Bellan, L. M.; Craighead, H. Control of an Electrospinning Jet Using Electric Focusing and Jet-steering Fields. *J. Vac. Sci. Technol., B: Microelectron. Nanometer Struct. Process., Meas., Phenom.* **2006**, *24* (6), 3179−3183.

(13) Lee, J.; Jang, J.; Oh, H.; Jeong, Y. H.; Cho, D.-W. Fabrication of a Three-dimensional Nanofibrous Scaffold with Lattice Pores Using Direct-write Electrospinning. *Mater. Lett.* **2013**, *93*, 397−400.

(14) Zheng, G.; Li, W.; Wang, X.; Wu, D.; Sun, D.; Lin, L. Precision Deposition of a Nanofibre by Near-field Electrospinning. *J. Phys. D: Appl. Phys.* **2010**, *43* (41), 415501.

(15) Chang, C.; Limkrailassiri, K.; Lin, L. Continuous Near-field Electrospinning for Large Area Deposition of Orderly Nanofiber Patterns. *Appl. Phys. Lett.* **2008**, *93* (12), 123111.

(16) Brown, T. D.; Dalton, P. D.; Hutmacher, D. W. Melt Electrospinning Today: An Opportune Time for an Emerging Polymer Process. *Prog. Polym. Sci.* **2016**, *56*, 116−166.

(17) Visser, J.; Melchels, F. P.; Jeon, J. E.; Van Bussel, E. M.; Kimpton, L. S.; Byrne, H. M.; Dhert, W. J.; Dalton, P. D.; Hutmacher, D. W.; Malda, J. Reinforcement of Hydrogels using Three-dimensionally Printed Microfibres. *Nat. Commun.* **2015**, *6*, 6933.

(18) Chen, F.; Hochleitner, G.; Woodfield, T.; Groll, J.; Dalton, P. D.; Amsden, B. G. Additive Manufacturing of a Photo-cross-linkable Polymer via Direct Melt Electrospinning Writing for Producing High Strength Structures. *Biomacromolecules* **2016**, *17* (1), 208−214.

(19) Farrugia, B. L.; Brown, T. D.; Upton, Z.; Hutmacher, D. W.; Dalton, P. D.; Dargaville, T. R. Dermal Fibroblast Infiltration of Poly (ε-caprolactone) Scaffolds Fabricated by Melt Electrospinning in a Direct Writing Mode. *Biofabrication* **2013**, *5* (2), 025001.

(20) Wright, N.; Humphrey, J. Denaturation of Collagen via Heating: an Irreversible Rate Process. *Annu. Rev. Biomed. Eng.* **2002**, *4* (1), 109−128.

(21) Kishi, N.; Iizuka, H. The Barus Effect of Polymer Melts. *J. Polym. Sci., Part B: Polym. Lett.* **1964**, *2* (4), 399−402.

(22) Hochleitner, G.; Jüngst, T.; Brown, T. D.; Hahn, K.; Moseke, C.; Jakob, F.; Dalton, P. D.; Groll, J. Additive Manufacturing of Scaffolds with Sub-micron Filaments via Melt Electrospinning Writing. *Biofabrication* **2015**, *7* (3), 035002.

(23) Abdul Rahman, N. Electrospun Conducting Polymer Nanofibers for Biomedical Applications. Thesis, University of Auckland, Auckland, New Zealand, 2012.

(24) Beumer, G.; Van Blitterswijk, C.; Bakker, D.; Ponec, M. Cell-seeding and in Vitro Biocompatibility Evaluation of Polymeric Matrices of PEO/PBT Copolymers and PLLA. *Biomaterials* **1993**, *14* (8), 598−604.

(25) Radder, A.; Leenders, H.; Van Blitterswijk, C. Application of Porous PEO/PBT Copolymers for Bone Replacement. *J. Biomed. Mater. Res.* **1996**, *30* (3), 341−351.

(26) Li, Z.; Wang, C. *One-Dimensional Nanostructures: Electrospinning Technique and Unique Nanofibers*; Springer, 2013.

(27) Heikkilä, P.; Harlin, A. Electrospinning of Polyacrylonitrile (PAN) Solution: Effect of Conductive Additive and Filler on the Process. *eXPRESS Polym. Lett.* **2009**, *3* (7), 437−445.

(28) Garg, K.; Bowlin, G. L. Electrospinning Jets and Nanofibrous Structures. *Biomicrofluidics* **2011**, *5* (1), 013403.

(29) Reneker, D. H.; Yarin, A. L. Electrospinning Jets and Polymer Nanofibers. *Polymer* **2008**, *49* (10), 2387−2425.

(30) De Vrieze, S.; Van Camp, T.; Nelvig, A.; Hagström, B.; Westbroek, P.; De Clerck, K. The Effect of Temperature and Humidity on Electrospinning. *J. Mater. Sci.* **2009**, *44* (5), 1357.

(31) Di Luca, A.; Lorenzo-Moldero, I.; Mota, C.; Lepedda, A.; Auhl, D.; Van Blitterswijk, C.; Moroni, L. Tuning Cell Differentiation into a

DOI: 10.1021/acsami.7b07151
ACS Appl. Mater. Interfaces 2017, 9, 38187−38200

3D Scaffold Presenting a Pore Shape Gradient for Osteochondral Regeneration. *Adv. Healthcare Mater.* **2016**, *5* (14), 1753−1763.
(32) Di Luca, A.; Szlazak, K.; Lorenzo-Moldero, I.; Ghebes, C. A.; Lepedda, A.; Swieszkowski, W.; Van Blitterswijk, C.; Moroni, L. Influencing Chondrogenic Differentiation of Human Mesenchymal Stromal Cells in Scaffolds Displaying a Structural Gradient in Pore Size. *Acta Biomater.* **2016**, *36*, 210−219.
(33) Nava, M. M.; Draghi, L.; Giordano, C.; Pietrabissa, R. The Effect of Scaffold Pore Size in Cartilage Tissue Engineering. *J. Appl. Biomater. Funct. Mater.* **2016**, *14* (3), e223−e229.
(34) Xu, J.; Abecassis, M.; Zhang, Z.; Guo, P.; Huang, J.; Ehmann, K.; Cao, J. Accuracy Improvement of Nano-fiber Deposition by Near-Field Electrospinning. *IWMF 9th International Workshop on Micro-factories*, 2014.
(35) Quan, X.; Ji, Y.; Zhang, H.; Zhang, Y.; Xu, X.; Zhong, T. Charging Compensation of Alumina Samples by Using an Oxygen Microinjector in the Environmental Scanning electron microscope. *Scanning* **2006**, *28* (5), 289−293.
(36) Ji, Y.; Guo, H.; Zhong, T.; Zhang, H.; Quan, X.; Zhang, Y.; Xu, X. Charge and Charging Compensation on Oxides and Hydroxides in Oxygen Environmental SEM. *Ultramicroscopy* **2005**, *103* (3), 191−198.
(37) Moroni, L.; De Wijn, J.; Van Blitterswijk, C. Three-dimensional Fiber-deposited PEOT/PBT Copolymer Scaffolds for Tissue Engineering: Influence of Porosity, Molecular Network Mesh Size, and Swelling in Aqueous Media on Dynamic Mechanical Properties. *J. Biomed. Mater. Res., Part A* **2005**, *75A* (4), 957−965.
(38) Steele, J.; McCullen, S.; Callanan, A.; Autefage, H.; Accardi, M.; Dini, D.; Stevens, M. Combinatorial Scaffold Morphologies for Zonal Articular Cartilage Engineering. *Acta Biomater.* **2014**, *10* (5), 2065−2075.
(39) Lien, S.-M.; Ko, L.-Y.; Huang, T.-J. Effect of Pore Size on ECM Secretion and Cell Growth in Gelatin Scaffold for Articular Cartilage Tissue Engineering. *Acta Biomater.* **2009**, *5* (2), 670−679.
(40) Tanaka, Y.; Yamaoka, H.; Nishizawa, S.; Nagata, S.; Ogasawara, T.; Asawa, Y.; Fujihara, Y.; Takato, T.; Hoshi, K. The Optimization of Porous Polymeric Scaffolds for Chondrocyte/atelocollagen Based Tissue-engineered Cartilage. *Biomaterials* **2010**, *31* (16), 4506−4516.
(41) Hendrikson, W. J.; Deegan, A. J.; Yang, Y.; van Blitterswijk, C. A.; Verdonschot, N.; Moroni, L.; Rouwkema, J. Influence of Additive Manufactured Scaffold Architecture on the Distribution of Surface Strains and Fluid Flow Shear Stresses and Expected Osteochondral Cell Differentiation. *Front. Bioeng. Biotechnol.* **2017**, *5*, DOI: 10.3389/fbioe.2017.00006.
(42) Athanasiou, K. A.; Rosenwasser, M.; Buckwalter, J.; Malinin, T.; Mow, V. Interspecies Comparisons of in Situ Intrinsic Mechanical Properties of Distal Femoral Cartilage. *J. Orthop. Res.* **1991**, *9* (3), 330−340.
(43) Mansour, J. M. Biomechanics of Cartilage. In *Kinesiology: The Mechanics and Pathomechanics of Human Movement*; Lippincott Williams & Wilkins: Philadelphia, PA, 2003; pp 66−79.
(44) Schinagl, R. M.; Gurskis, D.; Chen, A. C.; Sah, R. L. Depth-dependent Confined Compression Modulus of Full-thickness Bovine Articular Cartilage. *J. Orthop. Res.* **1997**, *15* (4), 499−506.
(45) Ghone, N. V.; Grayson, W. L. Recapitulation of Mesenchymal Condensation Enhances in Vitro Chondrogenesis of Human Mesenchymal Stem Cells. *J. Cell. Physiol.* **2012**, *227* (11), 3701−3708.
(46) Cao, B.; Li, Z.; Peng, R.; Ding, J. Effects of Cell−cell Contact and Oxygen Tension on Chondrogenic Differentiation of Stem Cells. *Biomaterials* **2015**, *64*, 21−32.
(47) Park, J. S.; Chu, J. S.; Tsou, A. D.; Diop, R.; Tang, Z.; Wang, A.; Li, S. The Effect of Matrix Stiffness on the Differentiation of Mesenchymal Stem Cells in Response to TGF-β. *Biomaterials* **2011**, *32* (16), 3921−3930.
(48) Minegishi, Y.; Hosokawa, K.; Tsumaki, N. Time-lapse Observation of the Dedifferentiation Process in Mouse Chondrocytes using Chondrocyte-specific Reporters. *Osteoarthritis and Cartilage* **2013**, *21* (12), 1968−1975.
(49) Hui, T.; Cheung, K.; Cheung, W.; Chan, D.; Chan, B. In Vitro Chondrogenic Differentiation of Human Mesenchymal Stem Cells in Collagen Microspheres: Influence of Cell Seeding Density and Collagen Concentration. *Biomaterials* **2008**, *29* (22), 3201−3212.
(50) Kobayashi, S.; Meir, A.; Urban, J. Effect of Cell Density on the Rate of Glycosaminoglycan Accumulation by Disc and Cartilage Cells in Vitro. *J. Orthop. Res.* **2008**, *26* (4), 493−503.
(51) Kiani, C.; Chen, L.; Wu, Y. J.; Yee, A. J.; yang, B. B. Structure and Function of Aggrecan. *Cell Res.* **2002**, *12* (1), 19−32.
(52) Sophia Fox, A. J.; Bedi, A.; Rodeo, S. A. The Basic Science of Articular Cartilage: Structure, Composition, and Function. *Sports health* **2009**, *1* (6), 461−468.
(53) Akiyama, H. Control of Chondrogenesis by the Transcription Factor Sox9. *Mod. Rheumatol.* **2008**, *18* (3), 213−219.
(54) Sekiya, I.; Tsuji, K.; Koopman, P.; Watanabe, H.; Yamada, Y.; Shinomiya, K.; Nifuji, A.; Noda, M. SOX9 Enhances Aggrecan Gene Promoter/Enhancer Activity and is Up-regulated by Retinoic Acid in a Cartilage-derived Cell Line, TC6. *J. Biol. Chem.* **2000**, *275* (15), 10738−10744.
(55) Hamilton, D. W.; Riehle, M. O.; Monaghan, W.; Curtis, A. S. Chondrocyte Aggregation on Micrometric Surface Topography: a Time-lapse Study. *Tissue Eng.* **2006**, *12* (1), 189−199.
(56) Wu, Y.-N.; Law, J. B. K.; He, A. Y.; Low, H. Y.; Hui, J. H.; Lim, C. T.; Yang, Z.; Lee, E. H. Substrate Topography Determines the Fate of Chondrogenesis from Human Mesenchymal Stem Cells Resulting in Specific Cartilage Phenotype Formation. *Nanomedicine* **2014**, *10* (7), 1507−1516.
(57) Oh, S. H.; Kim, T. H.; Im, G. I.; Lee, J. H. Investigation of Pore Size Effect on Chondrogenic Differentiation of Adipose Stem Cells Using a Pore Size Gradient Scaffold. *Biomacromolecules* **2010**, *11* (8), 1948−1955.
(58) Aigner, T.; Gebhard, P. M.; Schmid, E.; Bau, B.; Harley, V.; Pöschl, E. SOX9 Expression Does Not Correlate With Type II Collagen Expression in Adult Articular Chondrocytes. *Matrix Biol.* **2003**, *22* (4), 363−372.
(59) Sohier, J.; Vlugt, T.; Cabrol, N.; Van Blitterswijk, C.; De Groot, K.; Bezemer, J. Dual Release of Proteins from Porous Polymeric Scaffolds. *J. Controlled Release* **2006**, *111* (1), 95−106.
(60) DiGirolamo, C. M.; Stokes, D.; Colter, D.; Phinney, D. G.; Class, R.; Prockop, D. J. Propagation and Senescence of Human Marrow Stromal Cells in Culture: a Simple Colony-forming Assay Identifies Samples with the Greatest Potential to Propagate and Differentiate. *Br. J. Haematol.* **1999**, *107* (2), 275−281.
(61) Phinney, D. G.; Kopen, G.; Righter, W.; Webster, S.; Tremain, N.; Prockop, D. J. Donor Variation in the Growth Properties and Osteogenic Potential of Human Marrow Stromal Cells. *J. Cell. Biochem.* **1999**, *75* (3), 424−436.

NOTE ADDED AFTER ASAP PUBLICATION

This paper published ASAP on 10/28/2017. A duplicate set of author names was removed and the revised version was reposted on 11/8/2017.

DOI: 10.1021/acsami.7b07151
ACS Appl. Mater. Interfaces 2017, 9, 38187−38200